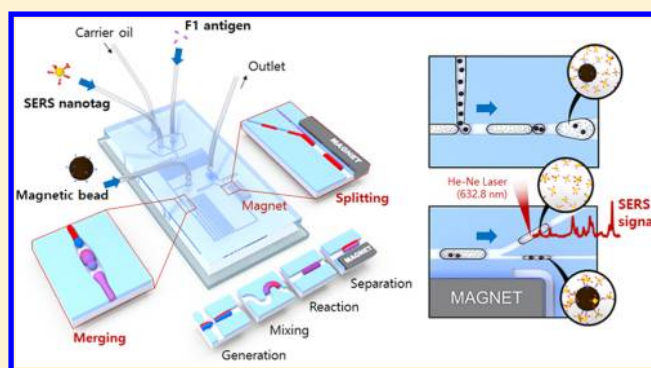


Integrated SERS-Based Microdroplet Platform for the Automated Immunoassay of F1 Antigens in *Yersinia pestis*Namhyun Choi,^{†,||} Jiyoung Lee,^{†,||} Juhui Ko,[†] Jun Ho Jeon,[‡] Gi-eun Rhie,[‡] Andrew J. deMello,^{*,§} and Jaebum Choo^{*,†,||}[†]Department of Bionano Technology, Hanyang University, Ansan 15588, South Korea[‡]Division of High-risk Pathogen Research, Center for Infectious Diseases, National Institute of Health, Cheongju 28159, South Korea[§]Department of Chemistry and Applied Biosciences, Institute of Chemical and Bioengineering, ETH Zürich, Vladimir Prelog Weg 1, 8093 Zürich, Switzerland

Supporting Information

ABSTRACT: The development of surface-enhanced Raman scattering (SERS)-based microfluidic platforms has attracted significant recent attention in the biological sciences. SERS is a highly sensitive detection modality, with microfluidic platforms providing many advantages over microscale methods, including high analytical throughput, facile automation, and reduced sample requirements. Accordingly, the integration of SERS with microfluidic platforms offers significant utility in chemical and biological experimentation. Herein, we report a fully integrated SERS-based microdroplet platform for the automatic immunoassay of specific antigen fraction 1 (F1) in *Yersinia pestis*. Specifically, highly efficient and rapid immuno-reactions are achieved through sequential droplet generation, transport, and merging, while wash-free immunodetection is realized through droplet-splitting. Such integration affords a novel multifunctional platform capable of performing complex multistep immunoassays in nL-volume droplets. The limit of detection of the F1 antigen for *Yersinia pestis* using the integrated SERS-based microdroplet platform is 59.6 pg/mL, a value approximately 2 orders of magnitude more sensitive than conventional enzyme-linked immunosorbent assays. This assay system has additional advantages including reduced sample consumption (less than 100 μ L), rapid assay times (less than 10 min), and fully automated fluid control. We anticipate that this integrated SERS-based microdroplet device will provide new insights in the development of facile assay platforms for various hazardous materials.



The development of rapid and sensitive screening methods for pathogenic bacteria in environmental or clinical samples is critical in the area of early diagnosis of infectious diseases or food-borne illnesses.^{1–3} Various detection methods, including bacteria colony counting, enzyme-linked immunosorbent assay (ELISA), and polymerase chain reaction (PCR), are considered to be the gold standards for the detection of pathogens.^{4–6} Unfortunately, these methods have serious drawbacks in terms of assay time and detection sensitivity. For instance, long culture times are required for bacteria colony counting, and similarly extended DNA amplifications are the norm in PCR. In the case of ELISA, unacceptably long assay times and poor detection limits are recognized as critical issues still to be resolved. Furthermore, these pathogen detection methods are ill-suited for in-the-field implementation because of inconvenient sampling and complicated instrumentation. Accordingly, there exists a pressing need for simple but efficient detection methods for the rapid and safe screening of pathogenic bacteria in contaminated environments or infected human blood.

Surface-enhanced Raman scattering (SERS)-based platforms are increasingly considered as promising formats for the detection of various biomarkers due to their high sensitivity and multiplex detection capability.^{7–13} When SERS nanotags are used as detection probes, their Raman scattering signals are greatly enhanced at active junctions known as “hot spots” due to both electromagnetic and chemical enhancement effects.^{14–16} Such enhancements have shown much promise in overcoming sensitivity problems inherent in the fluorescence or absorbance detection in ELISA or PCR assays. Moreover, SERS-based methods do not require culturing or amplification steps inherent to bacteria colony counting and PCR assays. To date, many different types of biomarkers including proteins,^{17–20} bacteria,^{21,22} and viruses^{23,24} have been studied using SERS-based assays. Of particular note are magnetic bead-based assays. Here, magnetic beads are used as a supporting

Received: May 16, 2017

Accepted: July 24, 2017

Published: July 24, 2017

substrate for the recognition of targets and also as an efficient tool for separation of magnetic immunocomplexes from the assay mixture.^{25–27}

Nonetheless, SERS-based assays using magnetic beads can be somewhat inconvenient due to problems associated with multiple manual washing steps, tedious manual handling of samples, and difficulties in controlling assay conditions.^{28,29} To resolve these problems, a microfluidic device has been introduced for automatic SERS-based immunoassays.^{30–32} Homogeneous mixing and sequential assay steps can be efficiently controlled within microfluidic channels, allowing rapid and highly sensitive SERS-based analyses. There are two primary types of flow regimes within such microfluidic platforms; namely continuous flow and segmented (or droplet) flow.^{33–36} Continuous flow systems are able to trap magnetic immunocomplexes with solenoids embedded inside microchannels but are ill-suited to washing unbound reagents under flow conditions. To resolve this problem, we recently developed a SERS-based microdroplet platform for wash-free immunoassays of prostate-specific antigen (PSA).³⁷ Within such droplet regimes, nanoliter-sized aqueous droplets containing sample reagents are encapsulated by a continuous oil phase. Primary droplets, including free and bound SERS nanotags, are segregated into two daughter droplets by magnetic forces, and the presence of PSA antigens leads to incorporation of more SERS tags in magnetic immunocomplexes and fewer SERS nanotags in the other supernatant droplets. In this way, the amount of PSA antigen can be precisely evaluated through SERS measurements in the separated droplets.

Despite the successful establishment of a wash-free assay system, a fully automatic microfluidic immunoassay platform is yet to be realized. To achieve this, multiple droplet manipulations for immunoreactions, washing of unbound reagents and detection of immunocomplexes must be performed in sequence. Herein, we design and fabricate a novel integrated microfluidic system that includes droplet generation, transport, mixing, merging, and splitting modules. The presented device allows efficient immunoreactions to be achieved through sequential droplet generation, transport, and merging, while wash-free immunoassays are realized through the droplet-splitting. This defines a conceptually new multifunctional microfluidic platform capable of performing a complex multistep immunoassays in nanoliter volumes for the safe and sensitive detection of hazardous materials. To validate our approach, the fraction 1 (F1) antigen for *Yersinia pestis*, which is of significant interest to the defense and security communities due to its potential use as a biological weapon, was chosen as a target protein marker.^{38,39}

EXPERIMENTAL SECTION

Materials and Chemicals. Gold(III) chloride trihydrate (>99.9%), sodium citrate dehydrate (99%), ethanolamine, 1H,1H,2H,2H-perfluorooctanol (PFO, 97%), trichloro-(1H,1H,2H,2H-perfluorooctyl) silane (97%), perfluorodecalin (PFD, 95%), dihydrolipoic acid (DHLA), EDC, and NHS were purchased from Sigma-Aldrich (MO, U.S.A.) and used without further purification. *Yersinia pestis* F1 antigen and anti-F1 antibody sets (capture and detection antibodies) were supplied by the Korea Center for Disease Control and Prevention. Phosphate-buffered saline (PBS; 10×, pH 7.4), 1 μm diameter carboxylic-activated magnetic beads (Dynabeads MyOne), and malachite green isothiocyanate (MGITC) were purchased from

Invitrogen Corporation (CA, U.S.A.). PDMS (Sylgard 184 Silicone Elastomer Kit) was purchased from Dow Corning (MI, U.S.A.). FC-40 (a mixture of perfluoro-trinbutylamine and perfluoro-di-*n*-butylmethylamine) and FC-70 (perfluorotriphenylamine) were purchased from 3M (MN, U.S.A.). A nickel-coated neodymium (ND) N45 magnet (5 × 2 × 1 mm³) was purchased from LG magnet (Seoul, Korea). Deionized water was purified using a Milli-Q water purification system (MA, U.S.A.).

Preparation of Polyclonal Anti-F1 Antibody-Conjugated SERS Nanotags. Au NPs were synthesized using the seeded-growth method reported by Bastús et al.⁴⁰ Briefly, 50 mL of 2.2 mM sodium citrate solution in a 100 mL, three-necked, round-bottomed flask was heated for approximately 15 min under vigorous stirring. Next, 50.0 μL of 25 mM HAuCl₄ solution was added to the flask upon boiling. The color of the solution changed from light yellow to bluish gray and then to soft pink within 10 min, indicating the formation of Au NPs. After the solution was boiled for a further 5 min, it was cooled to 90 °C. Subsequently, gold seeds were grown by sequentially injecting 500 μL of 60 mM sodium citrate and 500 μL of 25 mM HAuCl₄ solution 12 times at 2 min intervals. The solution was stirred continuously at 90 °C for 30 min. The resulting Au NPs were characterized by UV/vis absorption spectroscopy, DLS measurements, and TEM. The average diameter of the Au NPs was estimated to be 40 nm.

To prevent the aggregation of Au NPs during surface modification, 1.0 mL of 0.11 nM Au NPs colloidal solution and 10 μL of 36 μM Tween 20 were gently mixed for 15 min. Next, 1 μL of 0.1 mM MGITC was added to 1 mL of a Tween 20-treated Au NP colloidal solution, and the mixture reacted for 20 min under stirring. Antibody conjugation was induced by the addition of 2 μL of 0.1 mM DHLA. The two –SH functional groups of DHLA were cleaved and covalently bonded to the surfaces of the Au NPs. The solution was incubated for 1 h. The –COOH terminal groups on the surfaces of Au NPs were activated by adding 5 μL of 2.5 mM EDC and NHS. After 30 min, unreacted molecules were removed by centrifugation, and the remaining Au NPs were resuspended in PBS buffer solution. Afterward, 1 μL of 100 μg/mL *Yersinia pestis* anti-F1 polyclonal antibodies were reacted with the solution for 2 h at room temperature. Finally, unreacted sites on the surfaces of the Au NPs were deactivated by 2 μL of 1.0 mM ethanolamine for 20 min. Nonspecific binding chemicals and antibodies were washed through centrifugation, and the remaining SERS nanotags were resuspended in PBS buffer solution.

Preparation of Monoclonal Anti-F1 Antibody-Conjugated Magnetic Beads. To conjugate capture F1 antibodies onto the surfaces of magnetic beads, 400 μL of 0.5 mg/mL carboxylic group-functionalized magnetic beads were suspended in PBS buffer solution. Carboxylic groups on the surfaces of the magnetic beads were activated by 5 μL of 0.1 M EDC and NHS dissolved in distilled water for 30 min. Next, the magnetic beads were separated using a magnet and washed with PBS buffer solution to remove unreacted molecules. After the magnetic beads were resuspended with PBS buffer, 5 μL of 1 mg/mL anti-F1 monoclonal antibodies (4A7 mAb) was added to the magnetic bead solution and reacted for 2 h under stirring at room temperature. Anti-F1 monoclonal antibody-conjugated beads were washed three times to remove nonspecifically bound antibodies, followed by resuspension with PBS buffer solution.

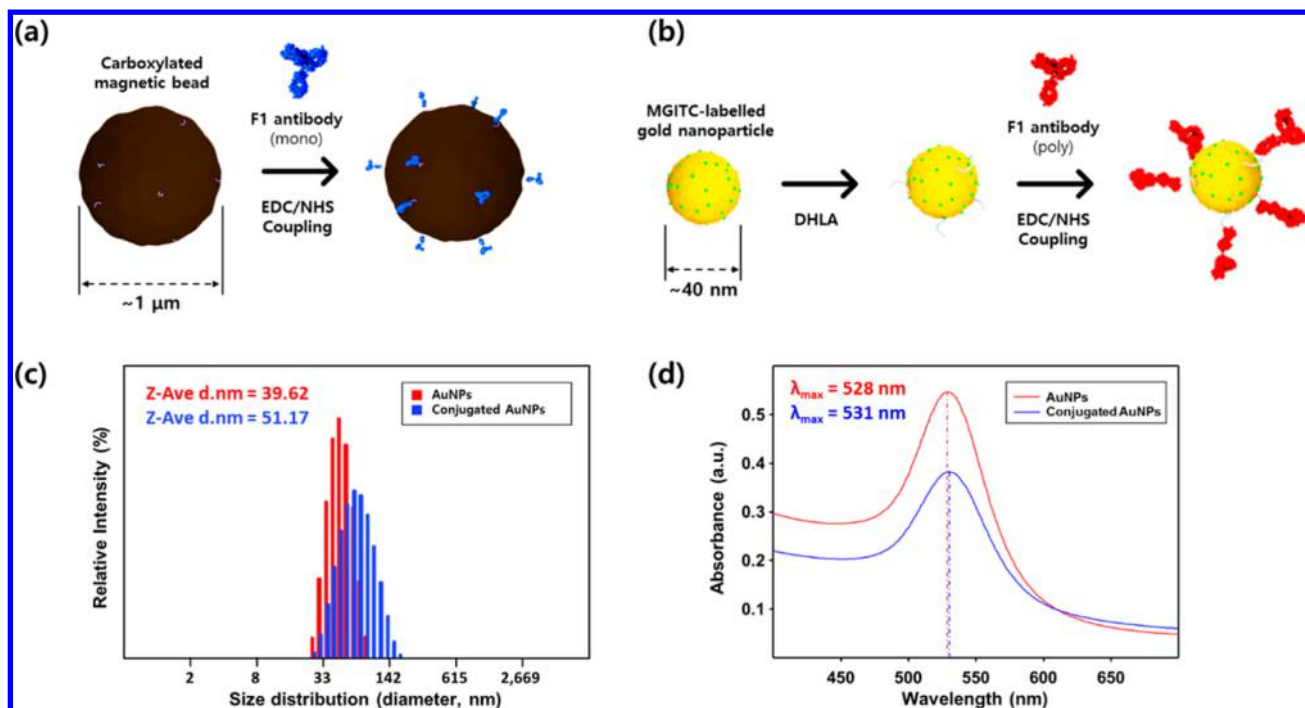


Figure 1. Schematic illustration of the fabrication processes of (a) monoclonal F1 antibody-conjugated magnetic beads and (b) polyclonal F1 antibody-conjugated SERS nanotags. Characterization of SERS nanotags: (c) dynamic light scattering distributions and (d) UV/visible spectra of Au NPs and F1 antibody-conjugated Au NPs.

Fabrication of the PDMS Microdroplet Sensor. The PDMS microfluidic device was fabricated by standard soft lithography and rapid prototyping methods. A positive SU-8 100 photoresist (Microchem Corporation) mold was fabricated on a silicon wafer using a transparent mask. The PDMS prepolymer and curing agent (Sylgard 184, Dow Corning) were mixed in a 10:1 ratio (w/w), degassed under vacuum, and then decanted onto the fabricated SU-8 mold. A neodymium magnet was placed in position, and the mixture was cured at 70 °C for 2 h in an oven. After curing, the PDMS replica was peeled from the master mold. Four inlet holes and one outlet hole were punched for fluidic access, and the PDMS replica was aligned to a glass slide in an oxygen plasma to form an irreversible bond. To increase the hydrophobicity of the inner channel walls, channels were filled with 1% (v/v) trichloro-(1H,1H,2H,2H-perfluorooctyl) silane in PFD solution, immediately after which the treated device was placed in an oven at 70 °C. The main channel was 200 μm wide, and the two branch channels were 140 and 70 μm wide, respectively. The width of the merging channel was 400 μm. The depth of all channels was 100 μm. A mixture of FC-40, FC-70, and PFO in a 10:20:3 (v/v) ratio was used as the carrier oil.

Imaging of Droplet Merging/Splitting and SERS Detection. An Olympus IX71 inverted fluorescence microscope (Olympus, Japan) equipped with a high-speed camera (PCO AG, Germany) was used to record droplet generation, merging, and splitting. Droplet volumes and velocities were measured using the same equipment. Precision syringe pumps (PHD 2000, Harvard Apparatus, U.S.A.), 1 mL Norm-Ject plastic syringes (Henke-Sass Wolf GmbH, Germany), 23 G needles (KOVAX-NEEDLE, Korea Vaccine Co., Ltd., Korea), and TYGON tubing (ID = 0.02 IN/OD = 0.06 IN, Saint-Gobain PPL Corp., France) were used to inject samples into the droplet channel. The SERS signals from droplets were collected using a Renishaw inVia Raman microscope system

(Renishaw, New Mills, UK). A 5 mW He–Ne laser operating at a 632.8 nm wavelength was used as the excitation source, and a charge-coupled device camera was combined with a spectrograph to provide a spectral resolution of 1 cm⁻¹. A 20× objective lens with a numerical aperture of 0.4 was used to focus the laser in the microdroplet channel. The Rayleigh line was removed using a holographic notch filter in the collection path. The exposure time was 10 s with two accumulations, and the focal laser spot size was 1.93 μm. Renishaw WiRE 4.0 software was used for data acquisition, control, and baseline correction. Since acquired spectra contain background noise, so the baseline correction is an important step in quantitative analysis. Here, a polynomial algorithm was used for each spectrum, and the baseline was corrected as zero. The flow rates were controlled simultaneously using three microsyringe pumps.

RESULTS AND DISCUSSION

Preparation of Antibody-Conjugated Magnetic Beads and SERS Nanotags. Figure 1a illustrates monoclonal F1 antibody conjugation on the surface of a carboxylated magnetic bead. Figure 1b shows the preparation of polyclonal F1 antibody-conjugated SERS nanotags. In both cases, the surface is activated by *N*-hydroxysuccinimide (NHS) and 1-ethyl-3-(3-(dimethylamino)propyl) carbodiimide (EDC), with monoclonal and polyclonal F1-antibodies subsequently being immobilized on magnetic beads and gold nanoparticles (Au NPs), respectively. The effects of antibody conjugation on the surface of the Au NPs were assessed by dynamic light scattering (DLS) and UV/visible (UV/vis) absorption measurements. As shown in Figure 1c,d, the average hydrodynamic size of Au NPs as measured by DLS increased from 40 to 51 nm upon conjugation, with the surface plasmon band shifting from 528 to 531 nm.

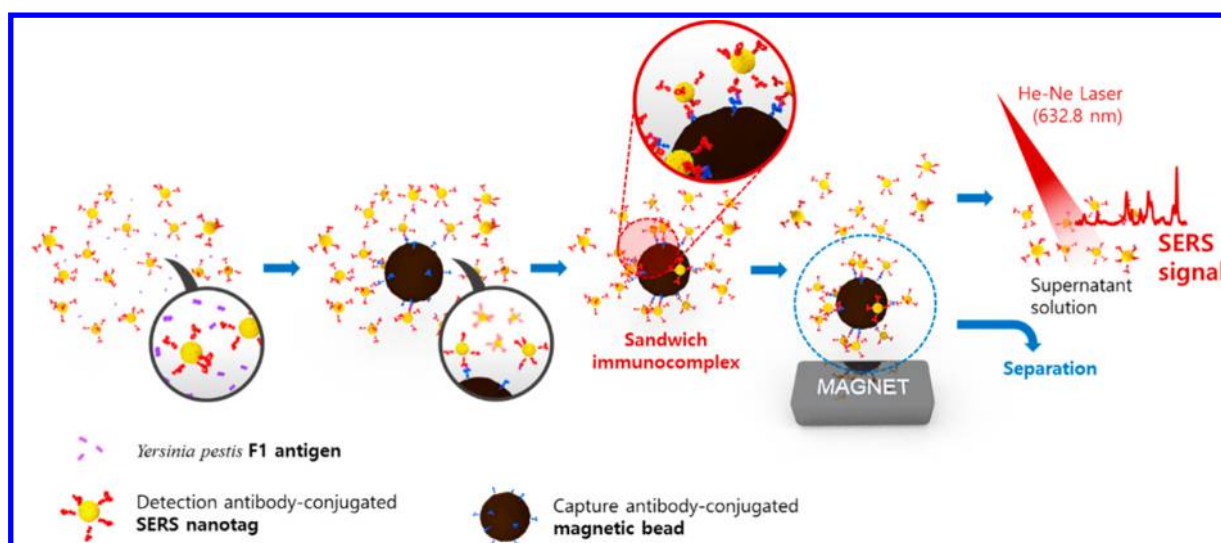


Figure 2. Schematic illustration of the SERS-based immunoassay platform for F1 antigen detection using SERS nanotags and magnetic beads.

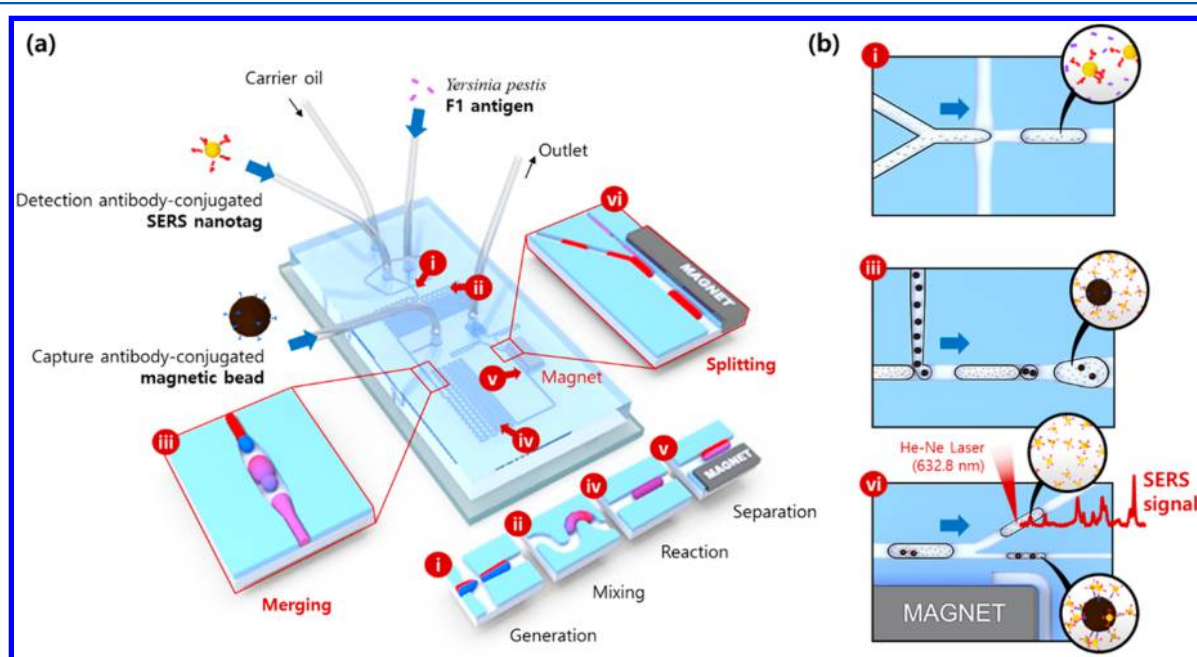


Figure 3. (a) Schematic design of the integrated SERS-based microfluidic channel composed of six microdroplet compartments: (i) droplet generation from the shear force at the interface between the aqueous and oil phases, (ii) droplet mixing for the first immunoreaction, (iii) droplet merging for the formation of magnetic immunocomplexes, (iv) droplet mixing for the second immunoreaction, (v) droplet splitting for the wash-free immunoassay, and (vi) Raman detection of unbound SERS nanotags in supernatant solution droplets. (b) Extended images for (i) droplet generation, (iii) droplet merging, and (vi) droplet splitting.

Formation of Magnetic Immunocomplexes for SERS-Based Immunoassay. Figure 2 details the formation of sandwich immunocomplexes and their SERS-based immunoassay. SERS nanotags and F1 antigens from *Yersinia pestis* were mixed with magnetic beads, and sandwich immunocomplexes were formed through antibody–antigen reaction. Subsequently, magnetic immunocomplexes were separated by a magnetic field and the SERS signals of the remaining nanotags were measured for the quantitative analysis of F1 antigens. Figure S1a shows the Raman spectra of the supernatant solution before and after the formation of magnetic immunocomplexes. In the absence of F1 antigen, sandwich magnetic immunocomplexes were not formed, and the corresponding Raman signal intensities of supernatant solution were accordingly strong. In the presence

of F1 antigen, magnetic immunocomplexes were formed, and the corresponding SERS signal intensities were greatly decreased. Figure S1b displays the corresponding transmission electron microscopy (TEM) images of a single magnetic bead before and after the formation of magnetic immunocomplexes.

Design and Fabrication of the SERS-Based Microdroplet Platform. To perform the immunoassay in a fully automatic fashion, a magnetic bar-embedded microchannel was designed and fabricated. It is important to note that since F1 antigens in *Yersinia pestis* and their corresponding antibodies are hazardous materials, rapid assays within enclosed environments are crucial for their safe detection.

Figure 3 illustrates the schematic design of the integrated microfluidic channel used in this study. The device consists of

six compartments. In the first compartment, aqueous solutions of the F1 antigens and anti-F1 (detection antibody)-conjugated SERS nanotags are supplied from two central inlets, and a carrier oil supplied orthogonally. Droplet formation results from shear forces at the interface between the aqueous and oil phases (top image in Figure 3b). In the second compartment, F1 antigens and anti-F1 SERS nanotags in each droplet are efficiently mixed by transport through multiple winding channels. Since the antibody–antigen reactions in each droplet are completely isolated, it is possible to perform the immunoreaction of hazardous materials safely as well as avoiding contamination from the surrounding environment. In the third compartment, anti-F1 (capture antibody)-conjugated magnetic beads are introduced into the inlet positioned at the middle of the chip, generating a second droplet. Subsequently, the first droplet (containing the F1 antigens and detection antibody-conjugated SERS nanotag mixtures) and the second droplet (containing capture antibody-conjugated magnetic beads) are sequentially merged through decompression in the wide merging channel (middle image in Figure 3b). In this geometry, the two droplets are pushed together before being pulled apart to initiate merging. To ensure efficient and robust merging, the flow rates of the two droplets must be precisely controlled. In the fourth compartment, immunoreactions between the capture antibody-conjugated magnetic beads and the antigen-captured SERS nanotags occur during passage through a second set of winding channels, with magnetic immunocomplexes being formed in a droplet twice as large as the originals.

In the fifth compartment, a magnetic bar embedded in the channel initiates droplet splitting. As shown in the bottom image of Figure 3b, magnetic immunocomplexes align on the bottom side of the droplet as each merged droplet passes close to the magnetic bar, while unreacted SERS nanotags and antigens in the supernatant solution remain on the other side of the droplet. Subsequently, each droplet is split into a pair of daughter droplets, which respectively contain primarily magnetic immunocomplexes and primarily unbound SERS nanotags. The critical parameter that controls droplet splitting under such conditions is the capillary number, which can be controlled by changing the droplet velocity, since the surface tension and the viscosities of both phases are constant. Specifically, the widths of the microchannels containing the two daughter droplets were varied to control both the droplet velocity and effective magnetic field strength. For the defined process, removal of unbound SERS nanotags and antigens by washing was not necessary since they are automatically separated from the magnetic immunocomplexes during droplet splitting. In the final compartment, both daughter droplets pass through a set of winding channels for the particle dispersion. Finally, Raman signals of the unbound SERS nanotags in the supernatant droplets are measured and analyzed for the quantitative analysis of F1 antigen. Movies S1, S2, and S3 show droplet merging for immunoreactions, droplet splitting for wash-free immunoassays, and the dispersion for immunodetection, respectively.

Optimization of the Flow Rate Ratio between Aqueous and Oil Phases. Figure 4a provides images of the entire microfluidic device and microchannel network, with Figure 4b,c illustrating the processes of droplet merging and splitting. Figure 4b also shows a sequence of images highlighting the merging of droplet streams, with the small downstream droplets containing captured magnetic beads and

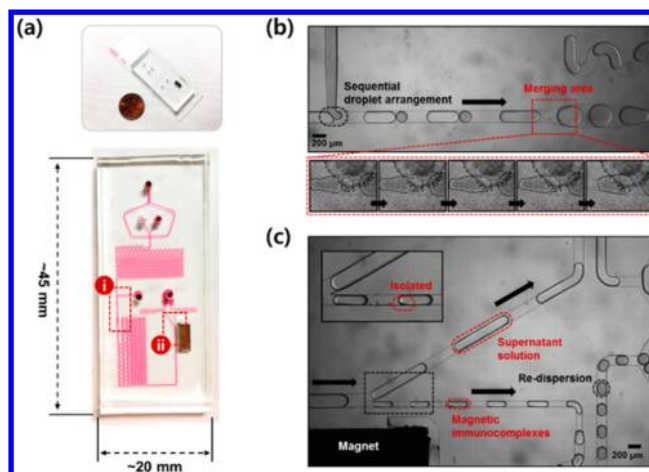


Figure 4. (a) Photographic images of the integrated microdroplet channel filled with red ink. Photographic images of the (b) droplet merging and (c) droplet splitting compartments. These images were captured by a high-speed camera installed in the microscope.

the larger upstream droplets containing SERS nanotags and F1 antigens. Figure 4c illustrates droplet-splitting for the wash-free immunoassay. Here, the flow rate ratio between the first aqueous and oil phases (Q_{aq1}/Q_{oil}) was varied to determine the optimal flow rate conditions for SERS enhancement as well as droplet merging. Specifically, the flow rate of the carrier oil phase was fixed at 2.0 $\mu\text{L}/\text{min}$, and the Q_{aq1}/Q_{oil} ratio was varied from 0.05 to 0.5. Figure S2a shows a series of images illustrating the droplet size changes associated with the variation in Q_{aq1}/Q_{oil} . Put simply, both droplet volume and droplet generation frequency increase with Q_{aq1}/Q_{oil} , as shown in Figure S2b,c. Critically, the SERS signal intensity also increases with Q_{aq1}/Q_{oil} , since the number of droplets passing through the detection probe volume per unit time increases. However, it was difficult to control alternative droplet merging conditions when Q_{aq1}/Q_{oil} exceeded 2.0. Thus, the optimal flow rates were determined to be 2.0 and 1.0 $\mu\text{L}/\text{min}$ for the carrier oil and the first aqueous stream, respectively. The flow rate of the second aqueous phase including magnetic beads was varied from 0.3 to 1.0 $\mu\text{L}/\text{min}$, with an optimal flow rate determined to be 0.6 $\mu\text{L}/\text{min}$.

Quantitative Analysis of F1 Antigen Using On-Chip SERS Detection. To monitor variations in the Raman intensity microdroplets moving along the channel, Raman spectra for 390 $\mu\text{g}/\text{mL}$ of F1 antigen were measured at four different channel positions (i–iv in Figure 5a). Figure 5a also displays the corresponding SERS spectra at these channel positions. The laser beam was focused into the center of a droplet, and Raman spectra were collected over 10 s at each channel position. The droplet merging and splitting processes were also monitored using a high-speed camera. The SERS signal intensity decreased slightly after droplet merging due to the decrease in SERS nanotag concentration in each droplet. After droplet splitting, the SERS signal intensity of the larger daughter droplets (including unbound SERS nanotags) was appreciably weaker than that of the smaller daughter droplets containing the sandwich magnetic immunocomplexes, as shown in Figure 5b. This is because most of the SERS nanotags were captured by the magnetic beads through antibody–antigen immune reactions.

Finally, a quantitative analysis of F1 antigen was carried out to evaluate assay performance at concentrations between 49.0

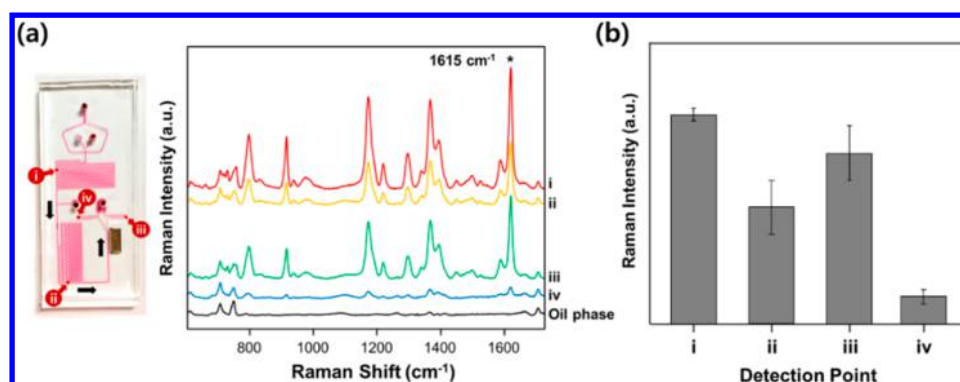


Figure 5. (a) Photographic image of the entire microfluidic channel and four laser focusing points (left). Corresponding Raman spectra at four different channel positions (right). The concentration of *Yersinia pestis* F1 antigen was 390 pg/mL. The Raman spectrum at each channel position was collected for 10 s, which encompassed the transit of about 200 droplets through the detection point. (b) Relative variations of Raman peak intensity centered at 1615 cm^{-1} along the channel.

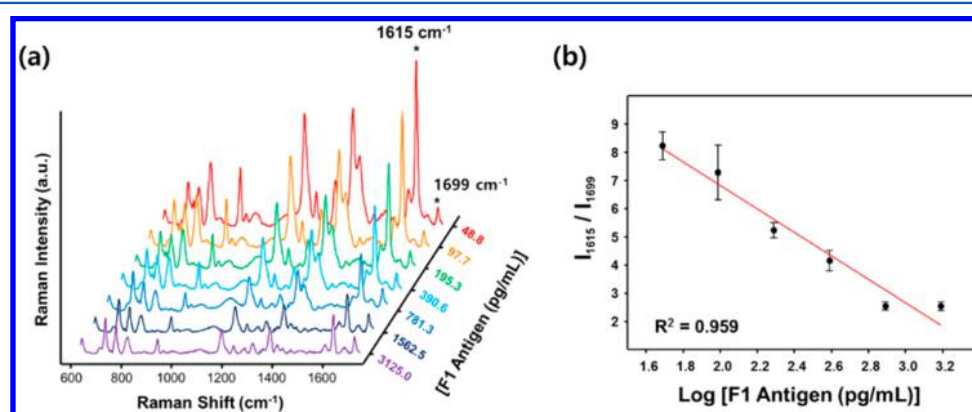


Figure 6. (a) Concentration-dependent SERS spectra of *Yersinia pestis* F1 antigen collected from the supernatant solution in microdroplets at channel position vi. The Raman spectrum at each channel position was collected for 10 s, which encompassed the transit of about 200 droplets through the detection point. (b) Corresponding log-scale calibration curve of the Raman intensity ratio (I_{1615}/I_{1699}) in the linear range as a function of F1 antigen concentration (correlation coefficient $R^2 = 0.959$). The error bars indicate the standard deviations of five measurements. Assay time: ~ 10 min.

pg/mL and 3.10 ng/mL. Figure 6a displays the associated Raman spectra for seven different antigen concentrations collected from the supernatant solution, including SERS nanotags in larger daughter droplets (position vi in Figure 3b). The SERS spectra at this channel position were collected for 10 s, which allowed analysis of approximately 200 droplets. To account for variations in laser power, local heating, and droplet size the Raman peak of the polydimethylsiloxane at 1699 cm^{-1} was used as an internal standard. Accordingly, the SERS intensity ratio (I_{1615}/I_{1699}) was determined for reproducible and quantitative evaluation of the *Yersinia pestis* F1 antigen. The resulting log-scale calibration curve in the linear range is displayed in Figure 6b. It can be seen that, as antigen concentration increases, the SERS intensity ratio decreases, because more SERS nanotags are captured by the magnetic beads with the increase in antigen concentration, and fewer SERS nanotags remain in the supernatant solution. In the positive assay (SERS detection for magnetic immunocomplexes), SERS intensity increases as antigen concentration increases because more SERS nanotags are captured by the magnetic beads with the increase of antigen concentration. In the negative assay (SERS detection for supernatant solution), however, SERS intensity decreases as antigen concentration increases because less unreacted SERS nanotags remain in the supernatant solution. In the case of positive assay, it is

impossible to completely remove unreacted SERS nanotags by the droplet splitting as shown in Figure 4c. Consequently, some parts of unreacted SERS nanotags are included in the droplets containing immunocomplexes, and this induces an error in the quantitative analysis of antigens. With this reason, we performed a negative assay for the supernatant solution.

The limit of detection (LOD) and correlation coefficient were estimated to be 59.6 pg/mL and 0.959, respectively. All error bars indicate standard deviations calculated from five measurements. Figure S3 shows ELISA-based assay results obtained from colorimetric analysis and a corresponding standard curve in the 0.5–1000 ng/mL range of F1 antigen. Here the color changes from dark green to colorless, as shown in Figure S3a. Figure S3b shows the standard curve for the formation of sandwich immunocomplexes at different F1 antigen concentrations. Again, standard deviations from five measurements are indicated by error bars. The LOD of F1 antigen determined by the ELISA method was approximately 2.3 ng/mL, a value 2 orders of magnitude less sensitive than the SERS-based assay. In addition, the LODs previously reported by other detection methods were also listed in Table S1 for comparison purposes. Accordingly, it can be concluded that the described droplet-based system can be successfully utilized for the rapid and sensitive immunoanalysis of F1 antigen.

CONCLUSION

In the current work, we have developed a multifunctional microfluidic platform composed of microdroplet merging and splitting compartments. The droplet merging and splitting compartments are used for efficient immunoreactions and wash-free detection, respectively. Such a novel microfluidic platform is also suitable for the analysis of other hazardous materials, since all of the immunoreaction and detection processes are performed in isolated nL-volumes in an automatic manner. Additionally, the device can be rapidly fabricated using soft-lithographic techniques, without the need for expensive microfabrication infrastructure.

We utilized this multifunctional microdroplet-based merging-splitting platform for the rapid, sensitive, and safe SERS-based immunoassay of F1 antigen in *Yersinia pestis* for the first time. The formation of magnetic immunocomplexes, composed of detection antibody-conjugated SERS nanotags-F1 antigen-capture antibody-conjugated magnetic beads, proceeded through a sequence of microdroplet generation, transport, merging, and splitting operations. Subsequently, large droplets including magnetic immunocomplexes were split into two daughter droplets for the wash-free immunoassay. For the highly sensitive and reproducible detection of unreacted SERS nanotags in the supernatant solution of the bigger daughter droplets, the Raman detection method has been adopted. The LOD of F1 antigen measured by using this SERS-based droplet merging and splitting microfluidic platform was estimated to be 59.6 pg/mL, which is approximately 2 orders of magnitude more sensitive than conventional gold-standard ELISA-based assays. Moreover, our approach consumes small volumes of sample (less than 100 μ L) and provides for fast assay time (less than 10 min). Such an integrated SERS-based microdroplet assay platform has obvious significant potential utility in the sensitive, rapid, and safe immunoanalysis of a range of hazardous materials.

ASSOCIATED CONTENT

Supporting Information

The Supporting Information is available free of charge on the ACS Publications website at DOI: 10.1021/acs.analchem.7b01822.

Additional figures and a table depicting experimental results as discussed in the text. (PDF)

Movie showing droplet merging for immunoreactions. (AVI)

Movie showing droplet splitting for wash-free immunoassays. (AVI)

Movie showing the dispersion for immunodetection. (AVI)

AUTHOR INFORMATION

Corresponding Authors

*E-mail: andrew.demello@chem.ethz.ch

*E-mail: jbchoo@hanyang.ac.kr

ORCID

Andrew J. deMello: 0000-0003-1943-1356

Jaebum Choo: 0000-0003-3864-6459

Author Contributions

^{||}N.C. and J.L. contributed equally.

Notes

The authors declare no competing financial interest.

ACKNOWLEDGMENTS

This work was supported by the Research Program of the Korea Centers for Disease Control and Prevention (Grant No. 2017E4500200). The National Research Foundation of Korea also supported this work (Grant Nos. 2008-0061891 and 2009-00426).

REFERENCES

- (1) Howes, P. D.; Chandrawati, R.; Stevens, M. M. *Science* **2014**, *346*, 1247390.
- (2) Howes, P. D.; Rana, S.; Stevens, M. M. *Chem. Soc. Rev.* **2014**, *43*, 3835–3853.
- (3) Chung, H. J.; Castro, C. M.; Im, H.; Lee, H.; Weissleder, R. *Nat. Nanotechnol.* **2013**, *8*, 369–375.
- (4) Pereiro, I.; Bendali, A.; Tabnaoui, S.; Alexandre, L.; Srbova, J.; Bilkova, Z.; Deegan, S.; Joshi, L.; Viovy, J. L.; Malaquin, L.; Dupuy, B.; Descroix, S. *Chem. Sci.* **2017**, *8*, 1329–1336.
- (5) Cassar, R.; Cuschieri, P. *J. Clin. Microbiol.* **2003**, *41*, 3229–3232.
- (6) Mothershed, E. A.; Whitney, A. M. *Clin. Chim. Acta* **2006**, *363*, 206–220.
- (7) Laing, S.; Gracie, K.; Faulds, K. *Chem. Soc. Rev.* **2016**, *45*, 1901–1918.
- (8) Lane, L. A.; Qian, X.; Nie, S. *Chem. Rev.* **2015**, *115*, 10489–10529.
- (9) Cao, Y. C.; Jin, R.; Mirkin, C. A. *Science* **2002**, *297*, 1536–1540.
- (10) Anker, J. N.; Hall, W. P.; Lyandres, O.; Shah, N. C.; Zhao, J.; Van Duyne, R. P. *Nat. Mater.* **2008**, *7*, 442–453.
- (11) Morla-Folch, J.; Xie, H. N.; Gisbert-Quilis, P.; Gomez-de Pedro, S.; Pazos-Perez, N.; Alvarez-Puebla, R. A.; Guerrini, L. *Angew. Chem., Int. Ed.* **2015**, *54*, 13650–13654.
- (12) Jiang, Z. Y.; Jiang, X. X.; Su, S.; Wei, X. P.; Lee, S. T.; He, Y. *Appl. Phys. Lett.* **2012**, *100*, 203104.
- (13) Granger, J. H.; Schlotter, N. E.; Crawford, A. C.; Porter, M. D. *Chem. Soc. Rev.* **2016**, *45*, 3865–3882.
- (14) Kneipp, K.; Kneipp, H.; Kneipp, J. *Acc. Chem. Res.* **2006**, *39*, 443–450.
- (15) Nie, S.; Emory, S. R. *Science* **1997**, *275*, 1102–1106.
- (16) Kneipp, K.; Kneipp, H.; Itzkan, I.; Dasari, R. R.; Feld, M. S. *Chem. Rev.* **1999**, *99*, 2957–2976.
- (17) Gracie, K.; Correa, E.; Mabbott, S.; Dougan, J. A.; Graham, D.; Goodacre, R.; Faulds, K. *Chem. Sci.* **2014**, *5*, 1030–1040.
- (18) Chon, H.; Lee, S.; Son, S. W.; Oh, C. H.; Choo, J. *Anal. Chem.* **2009**, *81*, 3029–3034.
- (19) Chon, H.; Lee, S.; Yoon, S. Y.; Lee, E. K.; Chang, S. I.; Choo, J. *Chem. Commun.* **2014**, *50*, 1058–1060.
- (20) Ye, J.; Chen, Y.; Liu, Z. *Angew. Chem., Int. Ed.* **2014**, *53*, 10386–10389.
- (21) Han, Z.; Liu, H.; Wang, B.; Weng, S.; Yang, L.; Liu, J. *Anal. Chem.* **2015**, *87*, 4821–4828.
- (22) Shao, F.; Lu, Z.; Liu, C.; Han, H.; Chen, K.; Li, W.; He, Q.; Peng, H.; Chen, J. *ACS Appl. Mater. Interfaces* **2014**, *6*, 6281–6289.
- (23) Paul, A. M.; Fan, Z.; Sinha, S. S.; Shi, Y.; Le, L.; Bai, F.; Ray, P. C. *J. Phys. Chem. C* **2015**, *119*, 23669–23775.
- (24) Costas, C.; Lopez-Puente, V.; Bodelon, G.; Gonzalez-Bello, C.; Perez-Juste, J.; Pastoriza-Santos, I.; Liz-Marzan, L. M. *ACS Nano* **2015**, *9*, 5567–5576.
- (25) Lee, S.; Chon, H.; Yoon, S. Y.; Lee, E. K.; Chang, S. I.; Lim, D. W.; Choo, J. *Nanoscale* **2012**, *4*, 124–129.
- (26) Huang, J.; Kim, K. H.; Choi, N.; Chon, H.; Lee, S.; Choo, J. *Langmuir* **2011**, *27*, 10228–10233.
- (27) Wu, L.; Wang, Z.; Fan, K.; Zong, S.; Cui, Y. *Small* **2015**, *11*, 2798–2806.
- (28) Pallaoro, A.; Hoonejani, M. R.; Braun, G. B.; Meinhart, C. D.; Moskovits, M. *ACS Nano* **2015**, *9*, 4328–4336.
- (29) Visaveliya, N.; Kohler, J. M. *Small* **2015**, *11*, 6435–6443.
- (30) Lee, M.; Lee, K.; Kim, K. H.; Oh, K. W.; Choo, J. *Lab Chip* **2012**, *12*, 3720–3727.

- (31) Wang, Y.; Vaidyanathan, R.; Shiddiky, M. J.; Trau, M. *ACS Nano* **2015**, *9*, 6354–6362.
- (32) Chon, H.; Lim, C.; Ha, S. M.; Ahn, Y.; Lee, E. K.; Chang, S. I.; Seong, G. H.; Choo, J. *Anal. Chem.* **2010**, *82*, 5290–5295.
- (33) Gu, S. Q.; Zhang, Y. X.; Zhu, Y.; Du, W. B.; Yao, B.; Fang, Q. *Anal. Chem.* **2011**, *83*, 7570–7576.
- (34) Brouzes, E.; Kruse, T.; Kimmerling, R.; Strey, H. H. *Lab Chip* **2015**, *15*, 908–919.
- (35) Niu, X.; Gulati, S.; Edel, J. B.; deMello, A. J. *Lab Chip* **2008**, *8*, 1837–1841.
- (36) Bremond, N.; Thiam, A. R.; Bibette, J. *Phys. Rev. Lett.* **2008**, *100*, 024501.
- (37) Gao, R.; Cheng, Z.; deMello, A. J.; Choo, J. *Lab Chip* **2016**, *16*, 1022–1029.
- (38) Papadopoulou, E.; Gale, N.; Goodchild, S. A.; Cleary, D. W.; Weller, S. A.; Brown, T.; Bartlett, P. N. *Chem. Sci.* **2015**, *6*, 1846–1852.
- (39) Papadopoulou, E.; Goodchild, S. A.; Cleary, D. W.; Weller, S. A.; Gale, N.; Stubberfield, M. R.; Brown, T.; Bartlett, P. N. *Anal. Chem.* **2015**, *87*, 1605–1612.
- (40) Bastus, N. G.; Comenge, J.; Puntès, V. *Langmuir* **2011**, *27*, 11098–11105.